An air-stable, reusable Ni@Ni(OH)2 nanocatalyst for CO2/bicarbonates hydrogenation to formate

Xin-Pu Fu, Laurent Peres, Jérôme Esvan, Catherine Amiens, Karine Philippot, Ning Yan

ARTICLE

An air-stable, reusable Ni@Ni(OH)$_2$ nanocatalyst for CO$_2$/bicarbonates hydrogenation to formate

Received 00th January 20xx,
Accepted 00th January 20xx

DOI: 10.1039/x0xx00000x

Xin-Pu Fu[a,‡] Laurent Peres[b,c,‡] Jérôme Esvan[d], Catherine Amiens[b,c], Karine Philippot*[,b,c], Ning Yan*[,a]

Production of formate via CO$_2$/bicarbonate hydrogenation using cheap metal-based heterogeneous catalysts is attractive. Herein, we report the organometallic synthesis of a foam-like Ni@Ni(OH)$_2$ composite nanomaterial which exhibited remarkable air stability and over 2 times higher catalytic activity than commercial Raney Ni catalyst in formate synthesis. Formate generation was reached with an optimal rate of 6.0 mmol/g$_{cat}$/h at 100°C, a significantly lower operation temperature compared to the 200-260°C reported in the literature. Deep characterization evidenced that this nanomaterial was made of an amorphous Ni(OH)$_2$ phase covering metallic Ni sites; a core-shell structure which is crucial for the stability of the catalyst. The adsorption of bicarbonates onto the Ni@Ni(OH)$_2$ catalyst was found a kinetically relevant step in the reaction, and the Ni-Ni(OH)$_2$ interface was found beneficial for both CO$_2$ and H$_2$ activation thanks to a cooperative effect. Our findings emphasize the underestimated potential of Ni-based catalysts in CO$_2$ hydrogenation to formate, pointing out a viable strategy to develop stable, cheap metal catalysts for greener catalytic applications.

Introduction

Carbon dioxide, as the main greenhouse gas, has severe impact on global warming and ocean acidification.[1-3] In parallel to limiting its release in the atmosphere, it is thus necessary to develop the capture of CO$_2$ and its utilization. Along with the gradual shift from fossil fuels to clean and renewable energy, CO$_2$ also represents a cheap, renewable carbon source for the future refinery.[4-7] Processes that convert CO$_2$ to valuable chemicals are thus of high interest for slowing down CO$_2$ accumulation in the atmosphere as well as generating chemicals from waste.[8-15]

Among various transformation approaches, conversion of CO$_2$ to formic acid (FA) or formate attracts considerable attention.[1, 16-22] FA is an important precursor for multiple organic chemicals.[24] Additionally, FA has potential as a hydrogen storage medium for fuel cell applications.[24-28] At present, a majority of reports focus on the transformation of CO$_2$ into formate *via* homogeneous catalytic systems,[15, 29-33] but the recycling and separation issues intrinsically associated with homogeneous catalysts limit their application in large scale. Concerning the production of formate from CO$_2$ over heterogeneous catalysts, the active elements are dominated by noble metals such as Ru,[16] Au[18] and Pd.[34-36] However, the use of precious metals as catalysts does not align well with the principles of sustainable chemistry, and thus it is desirable to develop catalytic systems based on cheaper and more abundant elements.

On account of their relatively low price and superior hydrogenation ability, nickel-based catalysts are attractive candidates to valorize CO$_2$.[9, 37, 38] Ni is well-known for CO$_2$ hydrogenation into methane, and also widely used in converting CO$_2$ and methane into syngas at high temperatures.[39-43] There is very limited research, however, exploring Ni-promoted hydrogenation of CO$_2$/bicarbonate into formate.[9, 44-46] Using Raney Ni as catalyst in the presence of amines, Farlow and Adkins observed the formation of amine/formic acid adducts from CO$_2$ and H$_2$.[46] Wang and co-workers reported that unsupported Ni promoted bicarbonate hydrogenation at relatively high temperature (200 °C).[45] As such, further development of synthetic protocols to prepare nickel-based catalysts active in CO$_2$ conversion into formate under milder conditions is needed. Since metallic nickel is easily oxidized when exposed to air, thus losing activity in hydrogenation, it is pivotal to design catalysts with enough stability without compromising their activity.

Herein, we report the one-step synthesis of a novel Ni@Ni(OH)$_2$ nanomaterial by an organometallic approach[47] using a commercial Ni precursor, the bis(cyclooctadiene) nickel(0) [Ni(COD)$_2$] complex. This new catalyst was

[a] Department of Chemical and Biomolecular Engineering, National University of Singapore, 4 Engineering Drive 4, Singapore, 117585, Singapore.
[b] CNRS, LCC (Laboratoire de Chimie de Coordination), 205 route de Narbonne, BP44099, F-31077 Toulouse Cedex 4, France.
[c] Université de Toulouse, UPS, INPT, F-31077 Toulouse CEDEX 4, France.
[d] CIRIMAT, CNRS-INP-UPS, INP-ENSIACET, 4 allée Emile Monso, BP 44362, F-31030, Toulouse Cedex 4, France.
‡ These authors contributed equally to this work.
Electronic Supplementary Information (ESI) available: [XPS, Raman, TGA, magnetic measurements, XRD, TEM, SEM, in-situ DRIFTS]. See DOI: 10.1039/x0xx00000x

characterized by a set of complementary techniques, including X-ray diffraction (XRD), Transmission and Scanning Electron Microscopy (TEM and SEM), X-ray photoelectron spectroscopy (XPS), Thermo Gravimetric Analysis (TGA) and magnetic measurements, and its activity was tested in the hydrogenation of CO_2 and bicarbonates in water. The results obtained afford new insight in the composition/structure/activity relationship and evidence the importance of both the Ni-Ni(OH)$_2$ interface and the amorphous character of the Ni(OH)$_2$ phase.

EXPERIMENTAL PART

Preparation of catalysts

Chemicals and gases: Argon and hydrogen were purchased from Air Liquide (Alphagaz). Tetrahydrofuran (THF) was obtained from CarloErba, purified using a purification MBraun SPS-800 machine and degassed with three freeze–pump-thaw cycles before use. Absolute anhydrous ethanol (CARLO ERBA Reagents, ACS reagent) was dried over molecular sieve and degassed by argon bubbling before further use. Bis(1,5-cyclooctadiene)nickel(0) (Ni(COD)$_2$) (>98%, Strem Chemicals) stored under argon inside the glovebox (MBraun). Deionized water was obtained from Millipore (MilliQ, 18.2 MΩ/cm; Millipore, Bedford, MA); Triethylamine (N(CH$_3$CH$_2$)$_3$, Sigma Aldrich Pte. Ltd); Sodium carbonate (Na$_2$CO$_3$, Aldrich); Sodium bicarbonate (NaHCO$_3$, Sigma Aldrich Pte. Ltd, ≥99.7%); Sodium hydroxide (NaOH, Sigma Aldrich Pte. Ltd); Potassium carbonate (K$_2$CO$_3$, Aldrich); Potassium bicarbonate (KHCO$_3$, Sigma Aldrich Pte. Ltd); Ammonium bicarbonate (NH$_4$HCO$_3$, Sigma Aldrich Pte. Ltd). Nickel(II) nitrate hexahydrate (Ni(NO)$_3$·6H$_2$O, Sigma Aldrich Pte. Ltd) were used as received.

Synthesis of Ni@Ni(OH)$_2$ nanomaterial. All the synthesis preparation was performed inside a glovebox or using schlenck tube techniques (Argon atmosphere). Typically, inside the glovebox, Ni(COD)$_2$ (4.0 mmol; 1.1 g) was added into a Fisher Porter (FP) bottle and solubilized in tetrahydrofuran (THF, 180 mL). Then, out of the glovebox, ethanol (20 mL, 10%v/v) was added with a syringe under argon. The FP bottle was subsequently pressurized with hydrogen (3 bar) and left under vigorous stirring at 70 °C for 20 h. After this period of time a black solid covering the stirring bar together with a colorless supernatant and a metallic mirror on the glassware were observed. Excess H_2 was then evacuated and the solvent evaporated under vacuum. The product was collected inside the glovebox using a magnet and scraping with a spatula and finally stored under inert atmosphere.

Synthesis of Ni@Ni(OH)$_{2[100\%ethanol]}$ The synthesis of this nanomaterial was done following the procedure described above for Ni@Ni(OH)$_2$ but using pure ethanol instead of a THF/EtOH 90/10 mixture .

Synthesis of Ni(OH)$_2$. In air Ni(NO)$_3$.6H$_2$O (0.725 g, 0.025 M) and urea (0.6 g, 0.1 M) were dissolved in 100 mL of de-ionized water. Then, the as-obtained solution was transferred into a round bottomed glass flask before refluxing at 90 °C for 6 h. After cooling down the reaction mixture, the obtained product was centrifuged and washed with de-ionized water for another 4 times. Subsequently, the as-formed solid was dried overnight at 120 °C in an oven to get the final product.[48]

Characterization Techniques

All the analyses on the samples before catalysis have been conducted under inert gas except for X-Ray Photoelectron Spectroscopy (XPS) and ThermoGravimetric Analysis (TGA). The crystallinity and phase purity of the samples were investigated by powder X-ray diffraction (XRD) on a Panalytical MPDPro diffractometer using Cu Kα radiation (λ = 1.5418 Å). Transmission electron microscopy (TEM) observation was carried out with a JEOL JEM 1400 microscope. The sample dispersion was made in isopropyl alcohol before deposition on a carbon-covered copper TEM grid. Scanning electron microscopy (SEM) was conducted on a JEOL 6700F microscope. The XPS spectra were collected by a Thermo Scientific K-Alpha system via using a monochromatised Al Kalpha (hν = 1486.6 eV) source. The size of the X-ray Spot was about 400 µm. The Pass energy was respectively fixed at 30 eV for core levels (step 0.1 eV) and 160 eV for surveys (step 1eV). The Au 4f7/2 (83.9 ± 0.1 eV) and Cu 2p3/2 (932.8 ± 0.1 eV) photoelectron lines were used to calibrate the spectrometer energy. All the XPS spectra were collected in direct mode N (Ec), coupling with subtraction of background signal via Shirley method. The charge effect was neutralized by using flood Gun on the top surface. The TGA was carried out with a Mettler Toledo TGA/DSC 3+ star system. The magnetic hysteresis curves were measured on a MPMS Quantum Design superconducting quantum interference device (SQUID) at 5 K between +5 and -5 T. Zero Field Cooled procedures (ZFC) or Field Cooled (FC) procedures under an applied field of 5 T where applied. The magnetization values are given per mass of material. Raman spectra were obtained using a laser Raman spectrometer Xplora from Horiba employing a laser with an incident wavelength of 532 nm. The CO_2-TPD (Temperature Programmed Desorption) profile was collected by mass spectra (MS, mass spectrometer (LC-D200M, TILON) with m/z = 44 (CO_2) under He flow. The sample was pre-treated at 100°C in purified N_2 (30 mL/min) for 30 min. Subsequently, the CO_2 molecules were adequately adsorbed on the samples with a flow rate of 30 mL/min at room temperature for another 1 h. After purging with He (30 mL/min) for another 1 h, desorption evolution was monitored by heating from 30 to 600 °C with a ramping rate of 10°C·min^{-1}. In situ DRIFTS (Diffuse Reflectance Infrared Fourier Transform Spectroscopy) tests were conducted on a commercial Nicolet iS50 FT-IR spectrometer, coupling with a reaction cell (Harrick Scientific Products, INC). With a scan number of 64 and at a resolution of 4 cm^{-1}, a mercury cadmium telluride (MCT)-A detector was used to record the spectra. The spectra were recorded at 100 °C and the spectrum of the background recorded in pure N_2 flow at the same temperature was subtracted.

Catalytic reaction

The CO_2/(bi)carbonate hydrogenation reactions to formate were performed in a batch reactor at various gas pressures and temperatures. Typically, 2 mL of ultrapure water was introduced into the reactor, and then 2 mmol of bicarbonate

($NaHCO_3$, $KHCO_3$, NH_4HCO_3) or carbonate (Na_2CO_3, K_2CO_3, $(NH_4)_2CO_3$) were added. After stirring for 1 min, the (bi)carbonate was dissolved completely. Then, the catalyst (10 mg) was added and dispersed uniformly into the solution via ultrasonic treatment for 5 min. Subsequently, either a CO_2/H_2 (1:1) gas mixture or pure H_2, at various pressures, was introduced into the reactor (the reactor was previously purged with CO_2/H_2 or H_2). Finally, the reactor was placed into an oil-bath and maintained at fixed temperature under stirring for 1 h. The concentration of reaction product ($HCOO^-$) was analyzed using ion chromatography equipment (Dionex ICS 5000 SP).

RESULTS AND DISCUSSION

The preparation of nanomaterials by the organometallic approach enables the generation of structurally well-defined catalysts. For example, the decomposition of the organometallic bis(cyclooctadiene) nickel(0) complex, ($Ni(COD)_2$), by H_2 leads to the formation of nickel nanoparticles with a controlled surface composition, depending on the ligand(s) and solvent(s) used.[47] Several applications of such nickel nanoparticles in catalysis have been published.[47, 49-53] In the present work we prepared a novel nickel nanomaterial by hydrogenation of the $Ni(COD)_2$ precursor in a THF/EtOH mixture in the absence of any additional stabilizer. As the only byproduct cyclooctane was eliminated under vacuum, no purification step of the obtained material was needed. As such, this synthesis method leads to a high purity catalyst without any residual halogen/nitrate/sulfide from the precursor that may poison the catalyst surface.[54] This allowed us to investigate the surface composition- and structure-activity relationships of this new nanomaterial in the catalytic hydrogenation of CO_2/(bi)carbonates to formate.

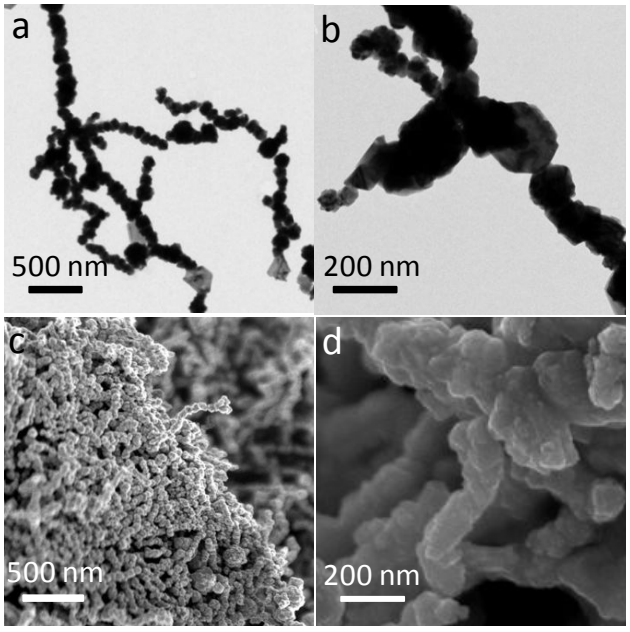

Fig. 1. TEM micrographs at (a) low magnification and (b) higher magnification; SEM micrographs at (c) low magnification and (d) higher magnification of as prepared $Ni@Ni(OH)_2$ foam.

The morphology of the as-prepared nickel nanomaterial (hereafter referred to as $Ni@Ni(OH)_2$ foam) was characterized by TEM and SEM. TEM analysis (Fig. 1a and 1b) showed Ni particles with a diameter of ca. 100 nm (100.3 ± 53.6 nm) aligned in worm-like structures. The SEM images (Fig. 1c and 1d) not only confirmed the approximate particle size of 100 nm with linear hierarchical organization but also revealed the foam-like character of the material. The nanomaterial surface exposed abundant kinks and edges, providing diverse possible active sites for catalysis.

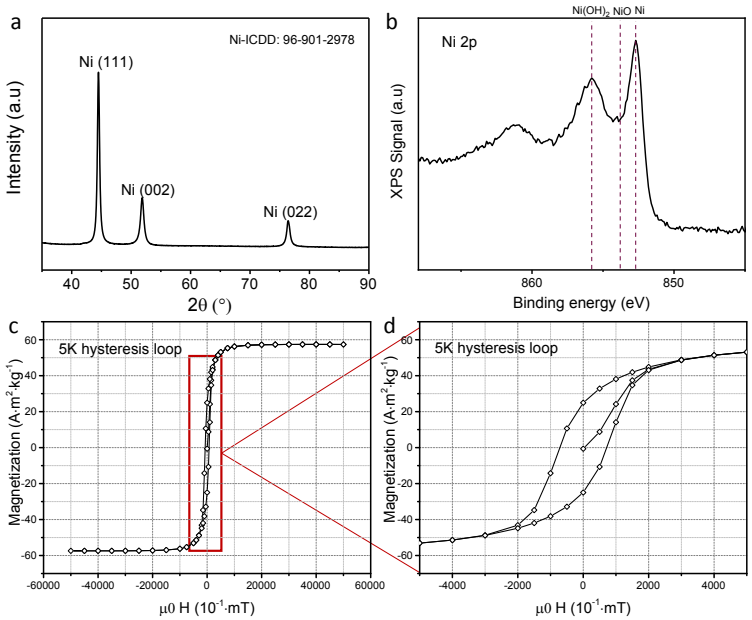

Fig. 2. (a) XRD pattern, (b) Ni 2p XPS spectrum (2p3/2 region) and (c, d) hysteresis cycle recorded at 5K (FC procedure under an applied field of 5T) on as prepared $Ni@Ni(OH)_2$ foam.

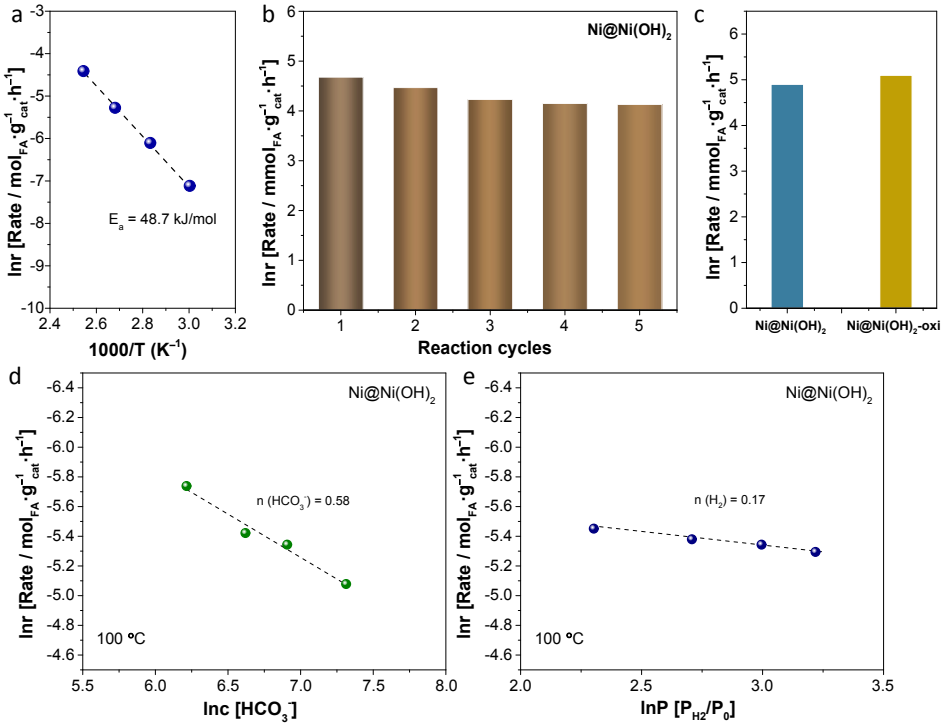

Fig. 3. (a) Apparent activation energy (E_a) of hydrogenation of $NaHCO_3$ over Ni@Ni(OH)$_2$ foam catalyst. (b) Recycling tests with Ni@Ni(OH)$_2$ foam catalyst for $NaHCO_3$ hydrogenation at 100 °C (1 h for each cycle). (c) Anti-oxidation test with Ni@Ni(OH)$_2$ foam catalyst for $NaHCO_3$ hydrogenation at 100 °C and Ni@Ni(OH)$_2$-oxi (catalyst treated under air at 90 °C for 24 h before catalytic test). Other reaction conditions: catalyst (10 mg) in 1 M aqueous $NaHCO_3$ solution, P_{H2} = 20 bar. Apparent reaction orders of (d) $NaHCO_3$ and (e) H_2 for $NaHCO_3$ hydrogenation reaction over Ni@Ni(OH)$_2$ foam catalyst.

The XRD pattern of Ni@Ni(OH)$_2$ foam shown in Fig. 2a matched well with the Ni(111), Ni(002) and Ni(022) peaks of the Ni fcc crystal structure as reported in Ni-ICDD:96-901-2978 data. An average crystallite size of 22.4 nm was determined using the Scherrer equation (mean size obtained over (111), (002) and (022) planes). This smaller crystallite size compared with the mean diameter of the particles measured in TEM images (ca. 100 nm) indicated that the nanomaterial was composed of individual nanocrystals of ca. 20-30 nm that were aggregated into regular superstructures of ca. 100 nm in size. The aggregation of these primary nanocrystals into large particles may be due to the weak surface interaction between ethanol or tetrahydrofuran, the only potential stabilizers present in the synthesis medium, while the wire-like morphology could be a consequence of the dipolar coupling between the magnetic particles induced by the magnet used to collect the material. XPS, an analytical technique identifying the near surface composition of materials (less than 10 nm in depth), was used to probe the composition of the nanomaterial. From literature, binding energies of 852.6 eV, 853.7 eV and 855.6 eV were ascribed to metallic Ni, NiO and Ni(OH)$_2$, respectively.[55, 56] As shown in Fig. 2b, the recorded Ni 2p spectrum showed two sharp peaks. The peak at 852.6 eV was attributed to metallic Ni and the second one, at 855.6 eV, was associated to Ni(OH)$_2$, clearly indicating the co-presence of metallic and hydroxide nickel species. NiO did not seem to exist in the surface layer.[57, 58] Based on these results, we hypothesized that the as-prepared nickel nanomaterial could be described as Ni@Ni(OH)$_2$, consisting of a layered structure with Ni(OH)$_2$ surrounding a metallic Ni core. The absence of Ni(OH)$_2$ diffraction peaks in the XRD diagram (Fig. 2a) indicated that the layer of Ni(OH)$_2$ was thin (≤1 nm) and/or amorphous. In the Raman spectrum (Fig. S1), six broad vibrational bands were observed between 300 and 900 cm^{-1} that were ascribed to different phases of Ni(OH)$_2$.[59] The more intense band at 520 cm^{-1} can derive from structural defects and/or correspond to a second order acoustic mode,[57, 60, 61] which supports the amorphous character of the Ni(OH)$_2$ layer in our nanomaterial.

The Ni@Ni(OH)$_2$ material was analyzed by TGA (Fig. S2). First, the sample was heated under air to 700 °C to remove organics while nickel was fully oxidized into NiO. After cooling down to 25 °C, the sample was placed under 2% H_2 flow and then heated again to 700 °C. Using this protocol, the Ni content was found to be close to 95%, indicating low organic, water and hydroxide contents. Magnetic properties were measured using a SQUID magnetometer, at 5 K with a field cooling sequence under 5 T (Fig. 2c and 2d), showing a perfectly symmetric hysteresis cycle. The results evidenced a ferromagnetic behavior with a saturation magnetization of 57.4 $A.m^2.kg^{-1}$ at 5 T and a coercive field of 140 mT. Interestingly, the value of the saturation magnetization was high and very close to that of bulk Ni (58.9 $A.m^2.kg^{-1}$). Considering the high Ni content measured by TGA (95%), this was in good agreement with the thin and amorphous character of the Ni(OH)$_2$ layer, since no exchange bias could be evidenced in the hysteresis loop (α-Ni(OH)$_2$ and β-Ni(OH)$_2$ are both antiferromagnetic at 5 K).[62, 63] When comparing with literature data,[63, 64] our nanomaterial displays high saturation magnetization and coercivity probably due to the linear organization of the particles coupled with the metallic Ni and amorphous Ni(OH)$_2$ magnetic properties. Additionally, the as-

prepared Ni@Ni(OH)$_2$ foam demonstrated remarkable resistance to oxidation even after a long period of time under ambient air. Indeed little change was observed in the magnetic properties (Fig. S3) of Ni@Ni(OH)$_2$ samples exposed to ambient air, with a limited and slow decrease of the metallic Ni content from 97.4% for the as-prepared Ni@Ni(OH)$_2$ to 94.5% and 93.4% for air-exposed samples after 3 and 21 weeks, respectively. Consistently, the XPS analysis of the materials surface after 21 weeks of air exposure (Fig. S4) showed an increase of the Ni(OH)$_2$ contribution and a decrease of metallic Ni one, thus indicating a thickened amorphous Ni(OH)$_2$ layer outside the metallic Ni cores.

The catalytic performance of the as-prepared Ni@Ni(OH)$_2$ foam-like nanomaterial was evaluated in the hydrogenation of $NaHCO_3$ into formate at 80°C in comparison with commercial Raney nickel and Ni catalysts in other forms (Table 1). The total mass of introduced catalyst was used to normalize the formate production rate. As shown in Table 1, in the absence of catalyst no formate was detected (entry 6). $Ni(NO_3)_2{\cdot}6H_2O$ and NiO were not effective for the hydrogenation of HCO_3^-. Commercial Raney Ni showed an activity of 0.9 mmol/g_{cat}/h (entry 2). The as-prepared Ni@Ni(OH)$_2$ foam catalyst showed a 2.5 times better performance than Raney Ni, reaching a value of 2.3 mmol/g_{cat}/h (entry 1). The catalytic activity was then evaluated at varied temperatures. The reaction rate increased to 4.7 mmol/g_{cat}/h at 100°C and reached 12.5 mmol/g_{cat}/h at 120°C (entries 7 and 8), which are milder reaction conditions than those previously reported for Ni-based catalysts.[9] The apparent activation energy of sodium bicarbonate hydrogenation has been determined as 48.7 kJ/mol (Fig. 3a).

Recycling tests of the Ni@Ni(OH)$_2$ foam catalyst were also performed under optimized conditions, namely at 100°C under 20 bar H_2. Between each catalytic run, the Ni@Ni(OH)$_2$ catalyst was washed with deionized water four times to eliminate residual substances. As shown in Fig. 3b, a high formate generation rate was still obtained after five catalytic cycles, indicating excellent stability and reusability of Ni@Ni(OH)$_2$ foam catalyst. To be noted, the activity of Ni@Ni(OH)$_2$ exhibited little change even after pre-treatment at 90°C under air for 24 h (sample referred to as Ni@Ni(OH)$_2$-oxi on Fig. 3c), further demonstrating its remarkable stability in air. In the XPS spectrum (Fig. S5), a high metallic Ni contribution was still detected in the surface layer after air treatment at 90°C, suggesting the presence of amorphous Ni(OH)$_2$ layer considerably slows down the oxidation of the metallic Ni core. This air stability is a plus regarding long term storage of this material.

When directly using CO_2 as a carbon source, a formate generation rate of ~6 mmol/g_{cat}/h was obtained at 100°C using NaOH as a base (entry 14, Table 1), slightly higher than in the case of HCO_3^-. This discrepancy in activity might be induced by an inhibited reverse reaction, namely the equilibrium of formate decomposition being suppressed by the presence of gaseous CO_2 and abundant OH^- in the solution. The activity is higher than that previously observed with Ni_3S_4 catalyst under similar conditions (~1 µmol/g_{cat}/h, reaction condition: 125 °C, 2MPa, CO_2/H_2 = 1:1),[65] but lower than those of Ni[45] and Ni-Zn[9] catalysts at 200 °C. GC analysis indicates the absence of volatile organic compounds such as methanol or acetic acid after reaction (Fig. S6), although methanol has been detected in trace amount in a previous study.[45] Using KOH as a base (entry 15, Table 1) led to an even higher value of 8.5 mmol/g_{cat}/h while NEt_3 led to a decreased activity (2.8 mmol/g_{cat}/h). Various bicarbonates and carbonates were screened as a carbon source (Table 1, entries 13-15). As a general trend, bicarbonates provided much higher activity than the corresponding carbonates. For instance, Na_2CO_3 only afforded an activity of 0.5 $mmol_{FA}{\cdot}g_{Cat}^{-1}{\cdot}h^{-1}$ as compared to $NaHCO_3$ that is almost ten times more active (entries 10 *vs* 7). Similar trend was found between K_2CO_3 and $KHCO_3$ (entries 11 vs 8). According to previous reports, it is more difficult to hydrogenate carbonates than bicarbonates as the result of the lower protonation of carbonate ions in the aqueous solutions.[66, 67] Among various bicarbonate salts, $NaHCO_3$ and $KHCO_3$ were equally effective affording high formate production rates of 4.7 and 4.8 $mmol_{FA}{\cdot}g_{Cat}^{-1}{\cdot}h^{-1}$, respectively (entries 7 and 8). In sharp contrast, the ammonium cation (NH_4^+, entry 10) showed an obvious negative influence in formate generation (0.3

Table 1. Catalytic performance of various catalysts in the hydrogenation of $NaHCO_3/CO_2$.

Entry	Substrates/ Solvent	Conditions[a]	Catalysts	Activity ($mmol_{FA}{\cdot}g_{Cat}^{-1}{\cdot}h^{-1}$)	TOF[b] (h^{-1})
1	$NaHCO_3$+H_2 /H_2O	80 °C, 20 bar	Ni@Ni(OH)$_2$	2.3	1.3
2	$NaHCO_3$+H_2 /H_2O	80 °C, 20 bar	Raney Ni	0.9	–
3	$NaHCO_3$+H_2 /H_2O	80 °C, 20 bar	Ni(OH)$_2$	0.2	–
4	$NaHCO_3$+H_2 /H_2O	80 °C, 20 bar	NiO	trace	–
5	$NaHCO_3$+H_2 /H_2O	80 °C, 20 bar	$Ni(NO_3)_2{\cdot}6H_2O$	trace	–
6	$NaHCO_3$+H_2 /H_2O	80 °C, 20 bar	Blank	trace	–
7	$NaHCO_3$+H_2 /H_2O	100 °C, 20 bar	Ni@Ni(OH)$_2$	4.7	2.6
8	$NaHCO_3$+H_2 /H_2O	120 °C, 20 bar	Ni@Ni(OH)$_2$	12.5	7.1
9	$KHCO_3$+H_2/ H_2O	100 °C, 20 bar	Ni@Ni(OH)$_2$	4.8	2.7
10	NH_4HCO_3+H_2/H_2O	100 °C, 20 bar	Ni@Ni(OH)$_2$	0.3	0.2
11	Na_2CO_3+H_2/ H_2O	100 °C, 20 bar	Ni@Ni(OH)$_2$	0.5	0.3
12	K_2CO_3+H_2/ H_2O	100 °C, 20 bar	Ni@Ni(OH)$_2$	0.6	0.3
13	$(NH_4)_2CO_3$+ H_2/H_2O	100 °C, 20 bar	Ni@Ni(OH)$_2$	0.1	0.06
14	CO_2+H_2/ NaOH	100 °C, 20 bar	Ni@Ni(OH)$_2$	6.0	3.4
15	CO_2+H_2/ KOH	100 °C, 20 bar	Ni@Ni(OH)$_2$	8.5	4.8
16	CO_2+H_2/ NEt_3	100 °C, 20 bar	Ni@Ni(OH)$_2$	2.8	1.6
17	CO_2+H_2/ H_2O	100 °C, 20 bar	Ni@Ni(OH)$_2$	1.7	0.9

[a]Reaction conditions in this work: catalyst (10 mg) in 1 M aqueous $NaHCO_3/KHCO_3/NH_4HCO_3/Na_2CO_3/K_2CO_3/(NH_4)_2CO_3$ (entries 1-13) or 1 M NaOH/KOH/NEt_3 solution; the CO_2:H_2 = 1:1 (entries 14-16).

[b]Turnover frequency (TOF) normalized by the percentage of exposed Ni atoms (10.2%) which was calculated using the average size of Ni crystallites determined from XRD analysis (Scherrer equation).[23]

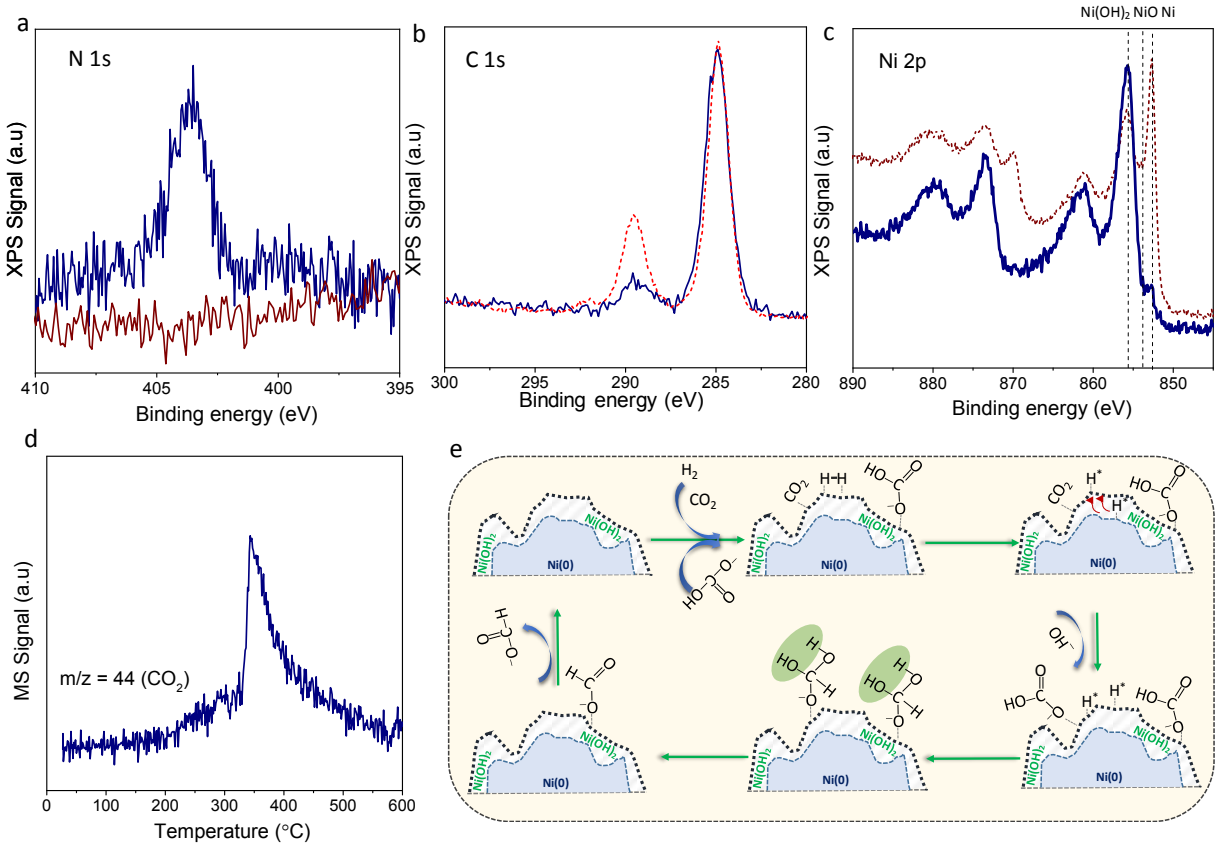

Fig. 4. (a) N 1s XPS spectrum of Ni@Ni(OH)$_2$ catalyst after reaction in NH_4HCO_3 (navy blue) and $NaHCO_3$ (red) solutions. (b) C 1s XPS spectrum of Ni@Ni(OH)$_2$ catalyst after NH_4HCO_3 (solid line) or $NaHCO_3$ (dash line) hydrogenation reaction. (c) Ni 2p XPS spectrum of Ni@Ni(OH)$_2$ foam catalyst after $NaHCO_3$ hydrogenation reaction (solid line). The dash line is the Ni 2p XPS spectrum of Ni@Ni(OH)$_2$ foam before $NaHCO_3$ hydrogenation reaction as comparison point. (d) CO_2-TPD profile of Ni@Ni(OH)$_2$ catalyst. (e) Schematic illustration of the plausible reaction pathway of CO_2 hydrogenation to formate over Ni@Ni(OH)$_2$ foam catalyst.

$mmol_{FA} \cdot g_{Cat}^{-1} \cdot h^{-1}$). Without base, formate was also generated despite of a lower formation rate (entry 17) indicating the potential role of surface hydroxide for the activation of CO_2.

To understand the origin of the cation effect, XPS spectra of the Ni@Ni(OH)$_2$ catalyst after reaction with NH_4HCO_3 and $NaHCO_3$ bicarbonates were compared (Fig. 4a and 4b). After reaction in NH_4HCO_3 solution (Fig. 4a), the observed N signal at 403.6 eV confirmed the presence of N-H bond of NH_4HCO_3 species on the surface of the spent catalyst (Ni@Ni(OH)$_2$-NH_4^+), which is absent for the Ni@Ni(OH)$_2$ catalyst after reaction in $NaHCO_3$ solution (Ni@Ni(OH)$_2$-$NaHCO_3$). In contrast, the intensity of the C 1s peak (Fig. 4b) for O–C=O species at ca. 289.0 eV on Ni@Ni(OH)$_2$-NH_4HCO_3 is weaker than that on Ni@Ni(OH)$_2$-$NaHCO_3$, indicating the lower adsorption of HCO_3^- on the surface of Ni@Ni(OH)$_2$ catalyst in the presence of NH_4^+. Therefore, despite $HCOONH_4$ (as-formed from NH_4HCO_3) is more readily decomposed into gaseous CO_2, NH_3 and H_2 as temperature increased, the negative effect observed seemed to derive from less accessible active sites due to the adsorption of NH_4^+ species at the catalyst surface that limited the adsorption and the reaction of HCO_3^-. This result points out the impact of the bicarbonate counter cation on the adsorption properties of the catalyst for the production of formate. Apparent reaction orders determined for $NaHCO_3$ and H_2 during the hydrogenation reaction of $NaHCO_3$ over Ni@Ni(OH)$_2$ foam catalyst was 0.58 for $NaHCO_3$, which is higher than the 0.17 obtained for hydrogen, also highlighting the essential role of the adsorption of bicarbonate species on the catalyst surface for hydrogenation.[19]

The XPS spectrum of Ni@Ni(OH)$_2$ catalyst collected after 1 h of reaction in $NaHCO_3$ solution was compared to that of the as-prepared catalyst (Fig. 4c). The two Ni 2p XPS spectra clearly showed a drastic decrease of the relative intensity of the peak at 852.6 eV corresponding to metallic Ni and a major contribution of the peak corresponding to Ni(OH)$_2$, centered at 855.7 eV after catalysis. These results indicated a composition evolution during the catalytic reaction leading to a higher proportion of Ni(OH)$_2$ in 10 nm thick surface layer probed by XPS. The stability of this hydroxide surface layer in Ni@Ni(OH)$_2$ catalyst was maintained after 5 test cycles, as confirmed by XPS analysis (Fig. S7). An XRD diagram recorded on the same spent catalyst (Fig. S8) showed only the classical Ni fcc pattern with a calculated crystallite size of 20.9 nm (Scherrer equation) thus indicating a slight decrease compared to crystallite size in the as-prepared nanomaterial (22.4 nm) but that metallic nickel is still present. Here again, no other diffraction peak than that of metallic Ni was observed indicating that the Ni(OH)$_2$ layer which continued to form at the surface of the material under catalytic conditions was amorphous. TEM and SEM images (Fig. S9 and S10, respectively) revealed a shell with a thickness larger than

10 nm covering the particle cores, which could be attributed to an amorphous $Ni(OH)_2$ phase.[57, 64] As this thickness is larger than the depth probed by XPS, it suggests that the Ni/$Ni(OH)_2$ interface is not regular with some Ni protuberances extending in the hydroxide layer or that some Ni islands are dispersed inside this layer. Although near surface metallic Ni is oxidized under the reaction conditions, which contributes to thicken the $Ni(OH)_2$ shell, this did not induce any appreciable drop in activity in five consecutive runs (Fig. 3b). As shown in Table 1 (entry 3), the crystallized $Ni(OH)_2$ material reference only demonstrated an activity of 0.2 $mmol_{FA}{\cdot}g_{Cat}^{-1}{\cdot}h^{-1}$ at 80 °C, which was obviously lower than that of Ni@$Ni(OH)_2$ foam catalyst where the hydroxide layer is amorphous (2.3 $mmol_{FA}{\cdot}g_{Cat}^{-1}{\cdot}h^{-1}$). Considering these, we propose that the metallic Ni in the core and the amorphous $Ni(OH)_2$ in the shell work cooperatively to convert CO_2 or bicarbonate to formate.

CO_2-TPD experiments were conducted to study the sorption ability of CO_2 on Ni@$Ni(OH)_2$ catalyst. As shown in Fig. 4d, one desorption peak was clearly observed at 400°C under helium atmosphere, indicating the effective capture ability for CO_2 at the catalyst surface. In-situ DRIFTS results indicated an apparent adsorbed CO_2 signal during the switching test between CO_2 and N_2 gas flow (Fig. S11). However, only a negligible signal of bicarbonate was observed in the range of 1000 to 1800 cm^{-1}, suggesting the relatively slow formation/adsorption rate of bicarbonate at the catalyst surface in good agreement with the higher reaction order of $NaHCO_3$ compared to H_2 (Fig. 3d).

On the basis of the present findings and previous reports,[19, 68] a simplified plausible reaction mechanism for carbon dioxide hydrogenation over Ni@$Ni(OH)_2$ foam catalyst is proposed in Fig. 4e, in which i) HCO_3^- and CO_2 species are adsorbed on amorphous $Ni(OH)_2$ while H_2 molecules diffuse to the metallic Ni core; ii) adsorbed CO_2 species are transformed to bicarbonates by reacting with the OH^- in the solution, or alternatively *via* reaction between gaseous CO_2 and hydroxide species present on the catalyst surface. In parallel, hydrogen dissociation happens on metallic Ni sites, followed by H spillover from metallic Ni to surface $Ni(OH)_2$; iii) one H atom attacks the carbon of the adsorbed bicarbonate and a second H atom links with the carbonyl O atom to form an unstable geminal diol and then a formate;[69] iv) the as-formed formate from CO_2 desorbs from the catalyst surface thus making the reaction enter into the next cycle. As the catalyst has a foam-like morphology along with an amorphous outside layer, the diffusion of H_2 may be facilitated. It is also worth mentioning, that based on the current experimental evidence, we cannot fully rule out the possibility that the amorphous $Ni(OH)_2$ surface is able to activate both H_2 and CO_2 without the direct participation of metallic Ni in the core.

Interestingly, we observed an increase in the catalytic activity of $NaHCO_3$ reduction to formate from 4.7 to 16.6 $mmol_{FA}{\cdot}g_{Cat}^{-1}{\cdot}h^{-1}$ at 100°C when synthesizing the nanomaterial in pure ethanol (sample named Ni@$Ni(OH)_{2[100\%ethanol]}$). The TEM and SEM results (Fig. S12) evidenced the presence of larger nanowires with a highly irregular surface. XPS and XRD data (Fig. S13) revealed a similar core-shell structure, but the Ni crystallite size decreased from ca. 21 nm to ca. 6 nm, suggesting that the higher activity observed with this catalyst derives from a size effect. Finally, as with the previous nanomaterial, this higher catalytic performance reinforces the unreleased potential of foam-like Ni@$Ni(OH)_2$ catalysts in CO_2 transformation.

Conclusion

We developed an air-stable, efficient and reusable Ni-based composite catalyst to generate formate *via* CO_2 hydrogenation. The foam-like Ni@$Ni(OH)_2$ nanomaterial was controllably and easily synthesized from a commercial organometallic compound without the use of stabilizer. The as-prepared catalyst exhibits a core-shell type structure with predominantly metallic Ni in the core and Ni/amorphous $Ni(OH)_2$ composite in the surface layer. The presence of the amorphous $Ni(OH)_2$ efficiently protected the catalyst against air oxidation, thus facilitating its long term storage. In CO_2/HCO_3^- hydrogenation, Ni@$Ni(OH)_2$ reached formate generation rate of 6.0/4.7 $mmol/g_{cat}/h$ at 100°C. By comparing formate generation rates using HCO_3^- and CO_3^{2-} as carbon source, and measuring apparent reaction orders, HCO_3^- was identified as the genuine precursor for formate synthesis. The co-existence of both metallic Ni and $Ni(OH)_2$ appeared to be crucial for both CO_2 and H_2 activation leading to high activity. The recycling study also evidenced excellent stability and reusability of Ni@$Ni(OH)_2$, with a high formate generation rate still observed after five catalytic cycles. This work reports a robust nickel-based nanomaterial that is a performant catalyst for CO_2 hydrogenation to formate, and contributes to the understanding of 'structure-activity' relationship in CO_2 conversion. Finally, the preliminary catalysis results obtained with the Ni@$Ni(OH)_{2[100\%ethanol]}$ nanomaterial, namely a reaction rate above 16.6 $mmol_{FA}{\cdot}g_{Cat}^{-1}{\cdot}h^{-1}$, indicate that higher catalytic performance can be reached by optimizing the catalyst design, i.e. by tuning the Ni domain sizes and Ni/$Ni(OH)_2$ interface.

Conflicts of interest

There are no conflicts to declare.

Acknowledgements

We are very grateful to Vincent Colliere (LCC-CNRS) for SEM observations, to Laure Vendier (LCC, CNRS) for XRD characterizations, to Marine Tasse (LCC-CNRS) for Raman measurements and to Jean-François Meunier (LCC-CNRS) for SQUID measurements. UMS 3623 - Centre de microcaractérisation Raimond Castaing is also thanked for electron microscopy equipment access. Funding information: the french National Agency for Research (project n°ANR-17-CE06-0017-01) and the Singapore National Research Foundation (WBS: R-279-000-530-281) are gratefully acknowledged for the financial support.

Notes and references

1 E. González, C. Marchant, C. Sepúlveda, R. García, I. T. Ghampson, N. Escalona and J. L. García-Fierro, *Appl. Catal. B: Environ.*, 2018, **224**, 368-375.
2 D. A. Bulushev and J. R. H. Ross, *Catal. Rev.*, 2018, **60**, 566-593.
3 A. Alvarez, A. Bansode, A. Urakawa, A. V. Bavykina, T. A. Wezendonk, M. Makkee, J. Gascon and F. Kapteijn, *Chem. Rev.*, 2017, **117**, 9804-9838.
4 S. Shyshkanov, T. N. Nguyen, F. M. Ebrahim, K. C. Stylianou and P. J. Dyson, *Angew. Chem. Int. Ed.*, 2019, **58**, 5371-5375.
5 H. Lin and E. J. Biddinger, *EnergyTech.*, 2017, **5**, 771-772.
6 M. Lu, J. Zhang, Y. Yao, J. Sun, Y. Wang and H. Lin, *Green Chem.*, 2018, **20**, 4292-4298.
7 C. Guan, Y. Pan, E. P. L. Ang, J. Hu, C. Yao, M.-H. Huang, H. Li, Z. Lai and K.-W. Huang, *Green Chem.*, 2018, **20**, 4201-4205.
8 J. M. Heltzel, M. Finn, D. Ainembabazi, K. Wang and A. M. Voutchkova-Kostal, *Chem. Commun.*, 2018, **54**, 6184-6187.
9 J. Wang, H. Jin, W. H. Wang, Y. Zhao, Y. Li and M. Bao, *ACS. Appl. Mater. Interfaces*, 2020, **12**, 19581-19586.
10 K. Mori, T. Sano, H. Kobayashi and H. Yamashita, *J. Am. Chem. Soc.*, 2018, **140**, 8902-8909.
11 L. Lombardo, H. Yang, K. Zhao, P. J. Dyson and A. Zuttel, *ChemSusChem*, 2020, **13**, 2025-2031.
12 A. Weilhard, M. I. Qadir, V. Sans and J. Dupont, *ACS Catal.*, 2018, **8**, 1628-1634.
13 M. I. Qadir, F. Bernardi, J. D. Scholten, D. L. Baptista and J. Dupont, *Appl. Catal. B: Environ.*, 2019, **252**, 10-17.
14 W. Leitner, *Angew. Chem. Int. Ed.*, 1995, **34**, 2207-2221.
15 K. Rohmann, J. Kothe, M. W. Haenel, U. Englert, M. Holscher and W. Leitner, *Angew. Chem. Int. Ed.*, 2016, **55**, 8966-8969.
16 K. Mori, T. Taga and H. Yamashita, *ACS Catal.*, 2017, **7**, 3147-3151.
17 T. Umegaki, Y. Enomoto and Y. Kojima, *Catal. Sci. Tech.*, 2016, **6**, 409-412.
18 G. A. Filonenko, W. L. Vrijburg, E. J. M. Hensen and E. A. Pidko, *J. Catal.*, 2016, **343**, 97-105.
19 Z. Zhang, L. Zhang, S. Yao, X. Song, W. Huang, M. J. Hülsey and N. Yan, *J. Catal.*, 2019, **376**, 57-67.
20 N. Yan and K. Philippot, *Curr. Opin. Chem. Eng.*, 2018, **20**, 86-92.
21 Y. Kuwahara, Y. Fujie, T. Mihogi and H. Yamashita, *ACS Catal.*, 2020, **10**, 6356-6366.
22 Z. Zhang, L. Zhang, M. J. Hülsey and N. Yan, *Mol. Catal.*, 2019, **475**, 110461.
23 M. Shekhar, J. Wang, W. S. Lee, W. D. Williams, S. M. Kim, E. A. Stach, J. T. Miller, W. N. Delgass and F. H. Ribeiro, *J. Am. Chem. Soc.*, 2012, **134**, 4700-4708.
24 F. Valentini, V. Kozell, C. Petrucci, A. Marrocchi, Y. Gu, D. Gelman and L. Vaccaro, *Energy Environ. Sci.*, 2019, **12**, 2646-2664.
25 M. Grasemann and G. Laurenczy, *Energy Environ. Sci.*, 2012, **5**, 8171-8181.
26 S. Masuda, K. Mori, Y. Futamura and H. Yamashita, *ACS Catal.*, 2018, **8**, 2277-2285.
27 B. Jin, X. Ye, H. Zhong and F. Jin, *ACS. Sustain. Chem. Eng.*, 2020, **8**, 6798-6805.
28 Z. Ni, H. Zhong, Y. Yang, G. Yao, B. Jin and F. Jin, *ACS. Sustain. Chem. Eng.*, 2019, **7**, 5827-5834.
29 C. A. Huff and M. S. Sanford, *ACS Catal.*, 2013, **3**, 2412-2416.
30 T. I. Philip G. Jessop, Ryoji Noyor, *Chem. Rev.*, 1995, **95**, 259-272.
31 Jing Cherng Tsai and K. M. Nicholas, *J. Am. Chem. Soc*, 1992, **114**, 5117-5124.
32 Ryo Tanaka, Makoto Yamashita and K. Nozaki, *J. Am. Chem. Soc.*, 2009, **131**, 14168–14169.
33 H. Li, T. P. Goncalves, Q. Zhao, D. Gong, Z. Lai, Z. Wang, J. Zheng and K. W. Huang, *Chem. Commun.*, 2018, **54**, 11395-11398.
34 Q. Sun, B. W. J. Chen, N. Wang, Q. He, A. Chang, C. M. Yang, H. Asakura, T. Tanaka, M. J. Hulsey, C. H. Wang, J. Yu and N. Yan, *Angew. Chem. Int. Ed.*, 2020, **132**, 20358 – 20366.
35 G. Liu, P. Poths, X. Zhang, Z. Zhu, M. Marshall, M. Blankenhorn, A. N. Alexandrova and K. H. Bowen, *J. Am. Chem. Soc.*, 2020, **142**, 7930-7936.
36 Q. Sun, X. Fu, R. Si, C. H. Wang and N. Yan, *ChemCatChem*, 2019, **11**, 5093-5097.
37 T. X. Sayle, S. C. Parker and D. C. Sayle, *Phys. Chem. Chem. Phys.*, 2005, **7**, 2936-2941.
38 C.-S. He, L. Gong, J. Zhang, P.-P. He and Y. Mu, *Journal of CO_2 Utilization*, 2017, **19**, 157-164.
39 C. V. Miguel, A. Mendes and L. M. Madeira, *Journal of CO_2 Utilization*, 2018, **25**, 128-136.
40 J. K. Kesavan, I. Luisetto, S. Tuti, C. Meneghini, G. Iucci, C. Battocchio, S. Mobilio, S. Casciardi and R. Sisto, *Journal of CO_2 Utilization*, 2018, **23**, 200-211.
41 M. Zhu, P. Tian, X. Cao, J. Chen, T. Pu, B. Shi, J. Xu, J. Moon, Z. Wu and Y.-F. Han, *Appl. Catal. B: Environ.*, 2021, **282**, 119561.
42 D. De Masi, J. M. Asensio, P. F. Fazzini, L. M. Lacroix and B. Chaudret, *Angew. Chem. Int. Ed.*, 2020, **59**, 6187-6191.
43 M. Romero-Sáez, A. B. Dongil, N. Benito, R. Espinoza-González, N. Escalona and F. Gracia, *Appl. Catal. B: Environ.*, 2018, **237**, 817-825.
44 Y. Zhao, T. Wang, X. Wang, R. Hao and H. Wang, *Chem. Eng. J.*, 2018, **347**, 860-869.
45 T. Wang, D. Ren, Z. Huo, Z. Song, F. Jin, M. Chen and L. Chen, *Green Chem.*, 2017, **19**, 716-721.
46 M. W. Farlow and H. Adkins, *J. Am. Chem. Soc.*, 1935, **57**, 2222–2223.
47 C. Amiens, B. Chaudret, D. Ciuculescu-Pradines, V. Collière, K. Fajerwerg, P. Fau, M. Kahn, A. Maisonnat, K. Soulantica and K. Philippot, *New J. Chem.*, 2013, **37**, 3374-3401.
48 M. Jayalakshmi, M. Mohan Rao and K.-B. Kim, *Int. J. Electrochem. Sci.*, 2006, **1**, 324-333.
49 N. J. S. Costa, M. Guerrero, V. Collière, É. Teixeira-Neto, R. Landers, K. Philippot and L. M. Rossi, *ACS Catal.*, 2014, **4**, 1735-1742.
50 A. Reina, I. Favier, C. Pradel and M. Gómez, *Adv. Synth. Catal.*, 2018, **360**, 3544-3552.
51 L. Zaramello, B. L. Albuquerque, J. B. Domingos and K. Philippot, *Dalton. Trans.*, 2017, **46**, 5082-5090.
52 T. Galeandro-Diamant, I. Suleimanov, L. Veyre, M. Bousquié, V. Meille and C. Thieuleux, *Catal. Sci. Tech.*, 2019, **9**, 1555-1558.
53 J. Zhang, M. Ibrahim, V. Collière, H. Asakura, T. Tanaka, K. Teramura, K. Philippot and N. Yan, *J. Mol. Catal. A: Chem.*, 2016, **422**, 188-197.
54 C. H.Bartholomew, *Studies in Surface Science and Catalysis*, 1987, **34**, 81-104.
55 A. N. Mansour, *Surface Science Spectra*, 1994, **3**, 231-238.
56 Hao Lei, Zhen Song, Dali Tan, Xinhe Bao, Xuhong Mu, Baoning Zong and E. Min, *Appl. Catal. A: General*, 2001, **214**, 69-76.
57 Y. Gao, H. Li and G. Yang, *Cryst. Growth Des.*, 2015, **15**, 4475-4483.
58 X. Ding, D. Fang, Z. Wang, H. Yang, J. Liu, Q. Deng, G. Ma, C. Meng, Y. Hu and H. H. Wen, *Nat. Commun.*, 2013, **4**, 1897.
59 D. S. Hall, D. J. Lockwood, S. Poirier, C. Bock and B. R. MacDougall, *J. Phys. Chem. A*, 2012, **116**, 6771-6784.
60 H. B. Li, M. H. Yu, F. X. Wang, P. Liu, Y. Liang, J. Xiao, C. X. Wang, Y. X. Tong and G. W. Yang, *Nat. Commun.*, 2013, **4**, 1894-1900.
61 P. Hermet, L. Gourrier, J. L. Bantignies, D. Ravot, T. Michel, S. Deabate, P. Boulet and F. Henn, *Phys. Rev. B*, 2011, **84**, 235211.
62 D. S. Hall, D. J. Lockwood, C. Bock and B. R. MacDougall, *Proc Math Phys Eng Sci*, 2015, **471**, 20140792.
63 T. Maity and S. Roy, *Journal of Magnetism and Magnetic Materials*, 2018, **465**, 100-105.

64 H. B. Li, P. Liu, Y. Liang, J. Xiao and G. W. Yang, *CrystEngComm*, 2013, **15**, 4054-4057.
65 C. Mitchell, D. Santos-Carballal, A. M. Beale, W. Jones, D. J. Morgan, M. Sankar and N. H. De Leeuw, *Faraday Discuss.*, 2021, DOI: 10.1039/d0fd00137f.
66 J. Su, M. Lu and H. Lin, *Green Chem.*, 2015, **17**, 2769-2773.
67 J. Su, L. Yang, M. Lu and H. Lin, *ChemSusChem*, 2015, **8**, 813-816.
68 J. Duo, F. Jin, Y. Wang, H. Zhong, L. Lyu, G. Yao and Z. Huo, *Chem. Commun.*, 2016, **52**, 3316-3319.
69 M. De Bruyn, V. L. Budarin, A. Misefari, S. Shimizu, H. Fish, M. Cockett, A. J. Hunt, H. Hofstetter, B. M. Weckhuysen, J. H. Clark and D. J. Macquarrie, *ACS Sustain. Chem. Eng.*, 2019, **7**, 7878-7883.